Nanoscale magnetic field imaging for 2D materials

Review Article

Author(s):
Marchiori, Estefani; Ceccarelli, Lorenzo; Rossi, Nicola; Lorenzelli, Luca; Degen, Christian L.; Poggio, Martino

Technical Review

Imaging weak magnetic field patterns on the nanometer-scale and its application to 2D materials

Estefani Marchiori[1], Lorenzo Ceccarelli[1], Nicola Rossi[1], Luca Lorenzelli[2], Christian L. Degen[2], and Martino Poggio[1,3,4]

Abstract

Nanometer-scale imaging of magnetization and current density is the key to deciphering the mechanisms behind a variety of new and poorly understood condensed matter phenomena. The recently discovered correlated states hosted in atomically layered materials such as twisted bilayer graphene or van der Waals heterostructures are noteworthy examples. Manifestations of these states range from superconductivity, to highly insulating states, to magnetism. Their fragility and susceptibility to spatial inhomogeneities limits their macroscopic manifestation and complicates conventional transport or magnetization measurements, which integrate over an entire sample. In contrast, techniques for imaging weak magnetic field patterns with high spatial resolution overcome inhomogeneity by measuring the local fields produced by magnetization and current density. Already, such imaging techniques have shown the vulnerability of correlated states in twisted bilayer graphene to twist-angle disorder and revealed the complex current flows in quantum Hall edge states. Here, we review the state-of-the-art techniques most amenable to the investigation of such systems, because they combine the highest magnetic field sensitivity with the highest spatial resolution and are minimally invasive: magnetic force microscopy, scanning superconducting quantum interference device microscopy, and scanning nitrogen-vacancy center microscopy. We compare the capabilities of these techniques, their required operating conditions, and assess their suitability to different types of source contrast, in particular magnetization and current density. Finally, we focus on the prospects for improving each technique and speculate on its potential impact, especially in the rapidly growing field of two-dimensional materials.

Introduction

In the early 1800s, images of the stray magnetic fields around permanent magnets and current-carrying wires made with tiny iron filings played a crucial role in the development of the theory of electromagnetism. Today, magnetic imaging techniques continue to provide invaluable insights well beyond producing pretty pictures. They shed light on magnetization patterns, spin configurations, and current distributions, which are invisible in optical or topographic images. Unlike bulk measurements of transport, magnetization, susceptibility, or heat capacity, they provide microscopic information about length-scales, inhomogeneity, and interactions. This kind of local information is proving crucial

[1] Department of Physics, University of Basel, 4056 Basel, Switzerland
[2] Department of Physics, ETH Zürich, 8093 Zürich, Switzerland
[3] Swiss Nanoscience Institute, University of Basel, 4056 Basel, Switzerland
[4] Email: martino.poggio@unibas.ch

38 in ongoing efforts to understand and harness an emerging class of two-dimensional (2D) van der Waals
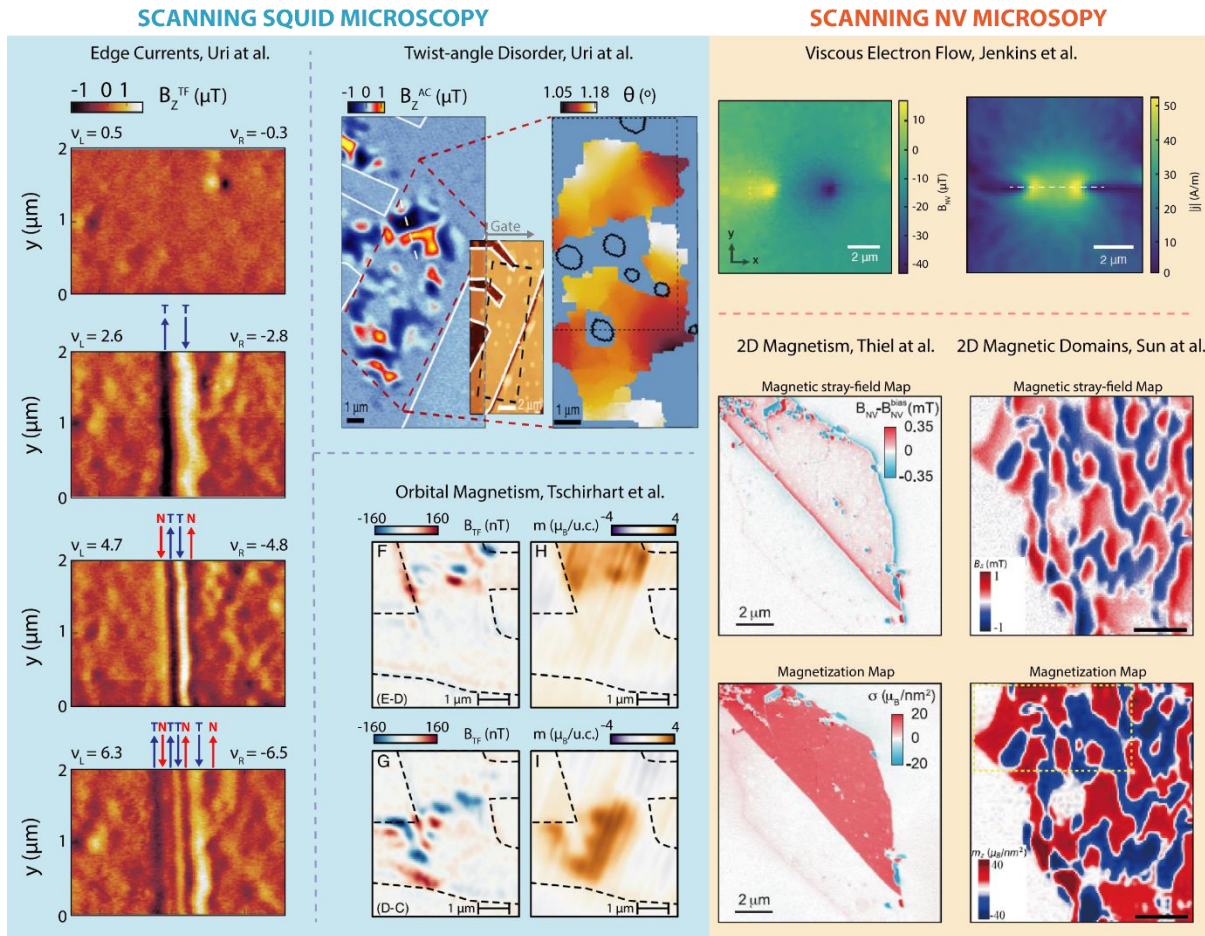39 (vdW) materials and their heterostructures.

40 The demonstration of the first graphene device in 2004 [1] launched the field of 2D and layered
41 materials. Graphene itself, however, represents just one of manifold atomically thin vdW materials
42 with a variety of compositions and crystal structures. Furthermore, heterostructures of these
43 materials can be engineered, due to the weak vdW interactions that typically dominate their interlayer
44 coupling: these interactions allow the stacking and twisting of individual atomically thin layers without
45 lattice mismatch adversely affecting the quality of the structure. This flexibility in both material choice
46 and structure design has led to the synthesis and fabrication of 2D materials with a range of properties
47 than span those of insulators, semiconductors, and metals.

48 Recent observations of correlation phenomena such as superconductivity, Mott insulating states, and
49 magnetically ordered states in such materials are particularly intriguing and are just beginning to be
50 understood. Such macroscopic manifestations of quantum mechanics are sensitive to the local
51 environment. In many cases, nanometer-scale spatial resolution is required to investigate and identify
52 the conditions for their emergence. As a result, there is now an urgent need for sensitive and high-
53 resolution imaging to zero-in on the nanometer-scale mechanisms behind these phenomena. In
54 particular, the techniques most adept at tackling this problem are scanning probe microscopies (SPMs)
55 designed to map subtle magnetic field patterns non-invasively. In 2D systems, such maps can be used
56 to image magnetization configurations and charge transport, giving crucial local information on
57 quantum phases, including on the spatial variation of order parameters, the presence of domains, and
58 the role of defects.

59 In the last few decades, the development of magnetic imaging technologies has been driven by
60 applications in magnetic storage and information processing. The need to understand magnetostatics
61 and dynamics on the nanometer-scale and with high temporal resolution has led to powerful optical,
62 electron, x-ray, and scanning probe microscopies. There are a number of excellent reviews on these
63 techniques and their myriad applications [2–7]. Most of these techniques, however, are not suitable
64 for resolving the weak contrast produced by both magnetization and current density in atomically thin
65 vdW materials.

66 This Technical Review focuses on the subset of state-of-the-art techniques best equipped for this
67 timely task. Scanning superconducting quantum interference device (SQUID) microscopy has already
68 demonstrated its ability to map superconducting currents [8] and magnetization [9] in magic-angle
69 twisted bilayer graphene (MATBG) or quantum Hall edge channels in mono-layer graphene [10,11].
70 Scanning nitrogen-vacancy (NV) center microscopy has been used to image layer-dependent
71 magnetization in Cr-based vdW magnets [12–14], as well as hydrodynamic electron flow in
72 graphene [15,16] and WTe_2 [17]. Sensitive forms of magnetic force microscopy (MFM), including
73 dissipation microscopy and nanowire (NW) MFM [18,19], are also poised to make an impact.

74 We treat these techniques in the following, briefly explaining how each works and specifying its
75 magnetic sensitivity and spatial resolution limits. We also touch on the process of reconstructing
76 spatial maps of measured magnetic field into images of magnetic moment or current. Finally, we
77 compare the different microscopies and speculate on which is most suitable for which type of contrast
78 and how each might best be applied in measurements of 2D materials.

Figure 1: Recent SPM measurements of magnetic field on 2D systems. On the left are measurements carried out by SSM (clockwise from top left): [8–10]; on the right by SNVM (clockwise from top): [12,13,15]. Measurements show magnetic field due both to magnetization and current density.
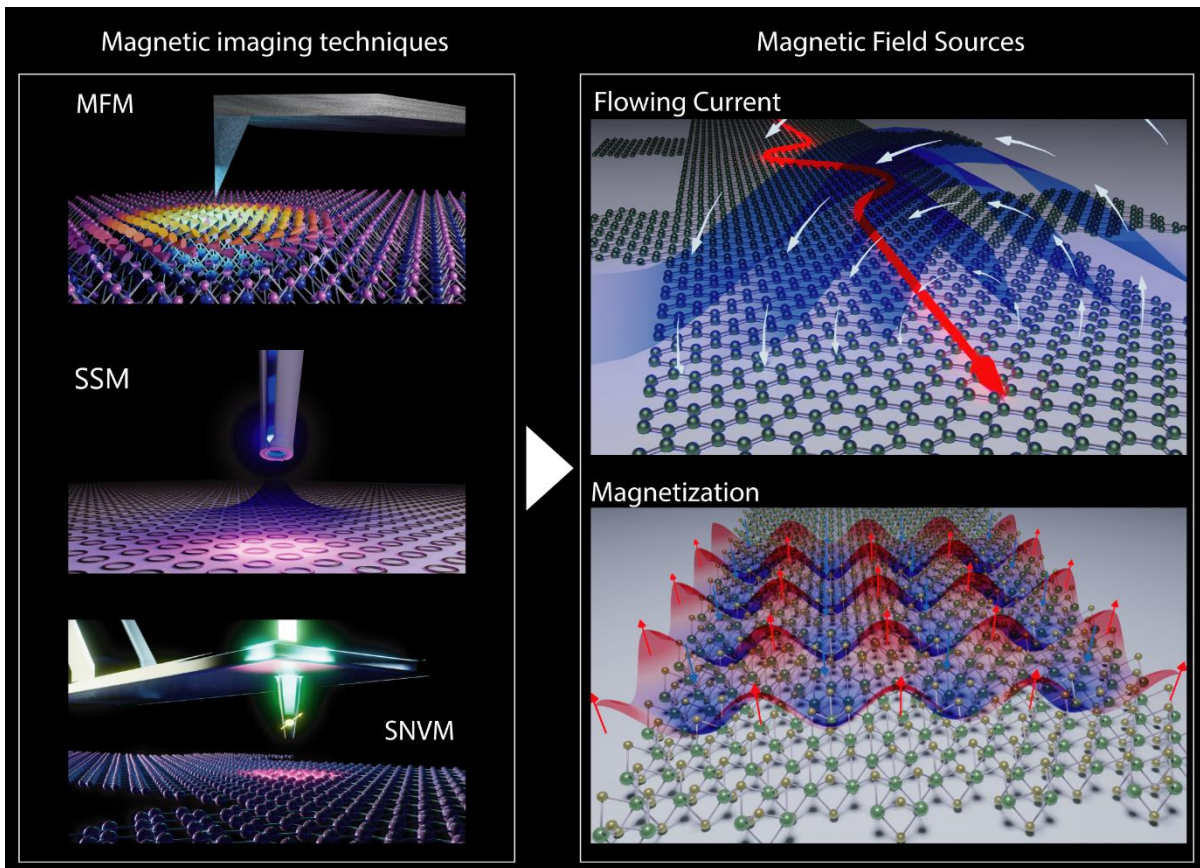
Imaging magnetization and current

Mapping magnetization patterns is important for investigations of magnetic domains, antiferromagnetism, magnetic skyrmion phases, and the spin-Hall effect. Measurements directly sensitive to magnetization include synchrotron-based x-ray techniques, neutron diffraction, and electron polarization techniques. For most, the tiny total magnetic moment of atomically-thin materials complicates their application to 2D systems. Particularly sensitive techniques such as magneto-optic microscopy and spin-polarized scanning tunneling microscopy have been used to reveal layer-dependent magnetism in flakes of CrI_3 [20] and films of $CrBr_3$, grown by molecular beam epitaxy [21], respectively. However, the spatial resolution of magneto-optical techniques is limited to the micrometer-scale and interference effects can obscure magnetic signals in thin samples. SP-STM requires atomically-clean conducting surfaces, which can often only be obtained by thermal annealing. Because many magnetic vdW materials are volatile at high temperatures, this step is sometimes not possible. Magnetic imaging via the magnetic circular dichroism of x-ray photoemission electron microscopy has not yet been applied to 2D systems. Nevertheless, its sensitivity should be sufficient to resolve single layer magnetism [22]. Huang et al. provide a recent survey on the application of magnetization-sensitive techniques to 2D materials and especially to 2D magnets [23].

Here, we consider techniques capable of mapping magnetic stray field, because they are applicable to a wider set of phenomena than direct magnetization imaging. Stray fields are produced not only by magnetization patterns, but also by current distributions. Transport imaging can be used to visualize local disorder, bulk and edge effects, electron guiding and lensing, topological currents, viscous electron flow, microscopic Meissner currents, and the flow and pinning of superconducting vortices. Common methods of mapping field include the use of fine magnetic powders as demonstrated by Bitter, Lorentz microscopy, electron holography, and a number of SPM techniques. Those most applicable to 2D systems, for their combination of high spatial resolution and high magnetic field sensitivity, are MFM, scanning SQUID microscopy (SSM), and scanning NV center microscopy (SNVM).

Although, in general, a map of magnetic field cannot be reconstructed into a map of the source current or magnetization distribution, under certain boundary conditions the source can be uniquely determined. In particular, for 2D structures such as 2D materials, patterned circuits, thin films, or semiconductor electron and hole gases, a spatial map of a single magnetic field component can be used to fully reconstruct the source current or out-of-plane magnetization distribution. Since some of the most interesting and elusive effects are observed over length-scales of less than 1 μm and with currents less than 1 μA or magnetizations of few μ_B/nm^2, techniques are required with both nanometer-scale spatial resolution and a sensitivity to fields smaller than a μT.

Figure 2: Schematic showing the principal magnetic imaging techniques and sources of magnetic field discussed in this review.

Imaging weak magnetic field patterns with high spatial resolution

In SPM, high spatial resolution is achieved by minimizing both sensor size and its distance from the sample. High sensitivity is obtained by maximizing signal-to-noise ratio for the magnetic signal of interest and the fundamental noise of the measurement. In evaluating the sensitivity of different techniques to magnetic contrast, we follow Kirtley [24] and consider their response to two idealized sources of magnetic field: a magnetic dipole moment and a line of current. This procedure allows us to assess and compare the sensitivity of each technique to magnetization and current density in a sample below.

Magnetic force microscopy

Working principle and conditions

Near surfaces, the most common technique for imaging magnetic fields with high spatial resolution is MFM, which was introduced in the late 1980s as a natural extension of atomic force microscopy [25,26]. Contrast results from the magnetostatic interaction between the stray magnetic fields of a sample and the magnetic tip of a mechanically compliant scanning probe. The vibration frequency and amplitude of a cantilever probe, whose tip has been coated with a ferromagnetic film, are recorded as the probe is scanned above a sample. The response typically depends on a gradient of the stray field. Although some simplifying assumptions can often be made, extracting exact magnetic field maps from MFM images involves a deconvolution requiring knowledge of the shape and magnetization configuration of the tip.

MFM is possible under a wide variety of conditions, including in air, liquid, vacuum, and over a broad range of temperatures. As shown in Fig. 3, a MFM system consists of the cantilever, piezoelectric positioners for moving the sample, and a setup for detecting cantilever motion, usually by optical deflection or interferometry. Scan areas are typically in the range of a few micrometers on a side and take several minutes. The cantilever's mechanical frequency, typically a few hundred kHz, sets the upper limit on the speed of the dynamics that can be measured. In fact, measurement bandwidths are limited to tens of Hz due to the linewidth of the mechanical resonance or the speed of the phase-locked loop used for determining the cantilever's frequency.

Cantilevers are typically made from Si, SiO_2, or Si_3N_4 and their tips are coated with a magnetic film of Co or Ni. Because cantilevers are optimized to probe surfaces on the atomic-scale, they are designed to have spring constants around 1 N/m, which is smaller but on the order of spring constant of an atomic bond at the surface of a solid. As a result, conventional MFM can have extremely high spatial resolution, down to 10 nm [27,28] at cryogenic temperatures and in vacuum, but more typically from 30 to 100 nm. This large spring constant, however, makes MFM responsive only to strong magnetic field modulations on the order of tens of $T/(m\ Hz^{1/2})$ (few µT over 100 nm measured in 1 s). It is, therefore, well-suited for the measurement of highly magnetized samples, however, ineffective for detecting the weak stray fields produced by subtle magnetization patterns or Biot-Savart fields of currents flowing through nanometer-scale devices.

The advent of cantilever probes consisting of individual nanowires (NWs) [29,30] or even carbon nanotubes [31] have given researchers access to much smaller force transducers. This reduction in size implies both a better force sensitivity and potentially a finer spatial resolution [32]. Sensitivity to small forces provides the ability to detect weak magnetic fields and therefore to image subtle magnetic patterns; tiny concentrated magnetic tips have the potential to achieve nanometer-scale spatial resolution, while also reducing the invasiveness of the tip on the sample under investigation.

NWs have been demonstrated to maintain force sensitivities around 1 $aN/Hz^{1/2}$ near sample surfaces (within 100 nm) when operated in high vacuum and at cryogenic temperatures, due to extremely low

166   noncontact friction [33]. In recent proof-of-principle experiments, both magnet-tipped NWs and fully
167   magnetic NWs were shown to be sensitive to magnetic field gradients of just a few mT/(m Hz$^{1/2}$) [10]
168   and a few nT/Hz$^{1/2}$ [19], respectively. These are the gradients and fields produced by tens of μ$_B$/Hz$^{1/2}$,
169   where μ$_B$ is a Bohr magneton, or several nA/Hz$^{1/2}$ of flowing current, each at a distance a hundred or
170   so nanometers.

171   *Sensitivity to different types of contrast*
172   Depending on the type of transducer and its tip, MFM maps magnetic field or magnetic field gradients.
173   The ultimate noise limiting these measurements is thermal noise acting on the transducer. Such noise
174   causes random fluctuations in the measured vibration amplitude and frequency. As shown in Box 1,
175   thermal noise sets a minimum measurable magnetic field or field gradient, depending on the
176   measurement type and the magnetization configuration of the tip. For example, a frequency shift
177   measurement of a conventional MFM transducer [34] has a thermal limit at 4 K to static gradients of
178   $\left(\frac{\partial B}{\partial r}\right)_{min} \approx 30$ T/(m Hz$^{1/2}$). Recently demonstrated NW MFM has a thermal limit for the same
179   measurement that is about 1000 times smaller [19].

180   *Box 1: MFM*
181   Force microscopy contrast is generated by the interaction of a cantilever tip with the sample
182   underneath. By monitoring the vibration amplitude, one can measure tip-sample forces at the
183   cantilever resonance frequency, while by monitoring the vibration frequency, one can measure static
184   tip-sample force gradients. The ultimate noise limiting these measurements is the thermal (Brownian)
185   motion of the cantilever. Thermal noise sets a minimum measurable resonant force $F_{min} = \sqrt{4\,k_B T\,\Gamma}$
186   in an amplitude measurement and a minimum measurable static force gradient $\left(\frac{\partial F}{\partial r}\right)_{min} =$
187   $\frac{1}{r_{rms}}\sqrt{4\,k_B T\,\Gamma}$ in a frequency measurement, where k_B is the Boltzmann constant, T is the
188   temperature, Γ is the mechanical dissipation, r_{rms} is the cantilever oscillation amplitude, and $\hat{r}$
189   indicates the direction of cantilever oscillation.

190   In MFM, the magnetic tip transduces a magnetic field profile into a force profile. This interaction can
191   often be approximated using a point-probe model, in which an effective magnetic multipole –
192   including a monopole q and a dipole $\boldsymbol{m}$ – represents the magnetization distribution of the tip. A
193   magnetic field profile $\boldsymbol{B}$ then produces a magnetic force acting on the cantilever given by $\boldsymbol{F}_{MFM} =$
194   $q\,\boldsymbol{B} \cdot \hat{r} + \nabla(\boldsymbol{m} \cdot \boldsymbol{B}) \cdot \hat{r}$. Note that, in most cases, the contribution of the torque generated by $\boldsymbol{B}$ is
195   negligible. For conventional MFM, where the tip-sample interaction can be approximated by a pure
196   magnetic monopole, this results in a minimum measurable resonant magnetic field $B_{min} =$
197   $\frac{1}{q}\sqrt{4\,k_B T\,\Gamma}$ and a minimum measurable static magnetic field gradient $\left(\frac{\partial B}{\partial r}\right)_{min} = \frac{1}{q\,r_{rms}}\sqrt{4\,k_B T\,\Gamma}$.
198   Purely dipolar tips, such as those on the ends of some NWs [18], are sensitive to a further spatial
199   derivative of the magnetic field, compared to monopolar tips. Similar expressions can be written
200   limiting those measurements.

201   By comparing the thermal noise background to the expected magnetic field or field gradient from a
202   single Bohr magneton μ_B or a line or current I, as calculated in Box 2, we can assess the sensitivity of
203   MFM. For example, conventional MFM scanning 50 nm above a sample is sensitive to frequency shifts
204   equivalent to a magnetic moment of a few thousand μ_B/Hz$^{1/2}$ or currents of a few μA/Hz$^{1/2}$ [34]. The
205   same type of measurement carried out with newly demonstrated NW MFM probes 100 nm above a
206   sample is about 100 times more sensitive to each type of contrast [18,19]. Estimates of sensitivity to
207   magnetic moment and current as a function of probe-sample spacing are shown in Figs. 4 a) and b).

208 It should be noted that the thermal limit on frequency measurements is rarely reached in practice.
209 Most frequency measurements are limited by other noise sources, such as temperature variations,
210 adsorption-desorption noise, or other microscopic mechanisms intrinsic to the resonator, that are
211 typically an order of magnitude larger [35]. On the other hand, measurements of resonant oscillation
212 amplitude, which are sensitive to modulations at the mechanical frequency of the sensor (typically in
213 the 100 kHz regime), are often thermally limited. In such measurements, conventional MFM
214 cantilevers can be sensitive to a few hundred $\mu_B/\mathrm{Hz}^{1/2}$ or a few hundred $\mathrm{nA/Hz}^{1/2}$, while NW MFM
215 transducers reach down to a few $\mu_B/\mathrm{Hz}^{1/2}$ or a few $\mathrm{nA/Hz}^{1/2}$.
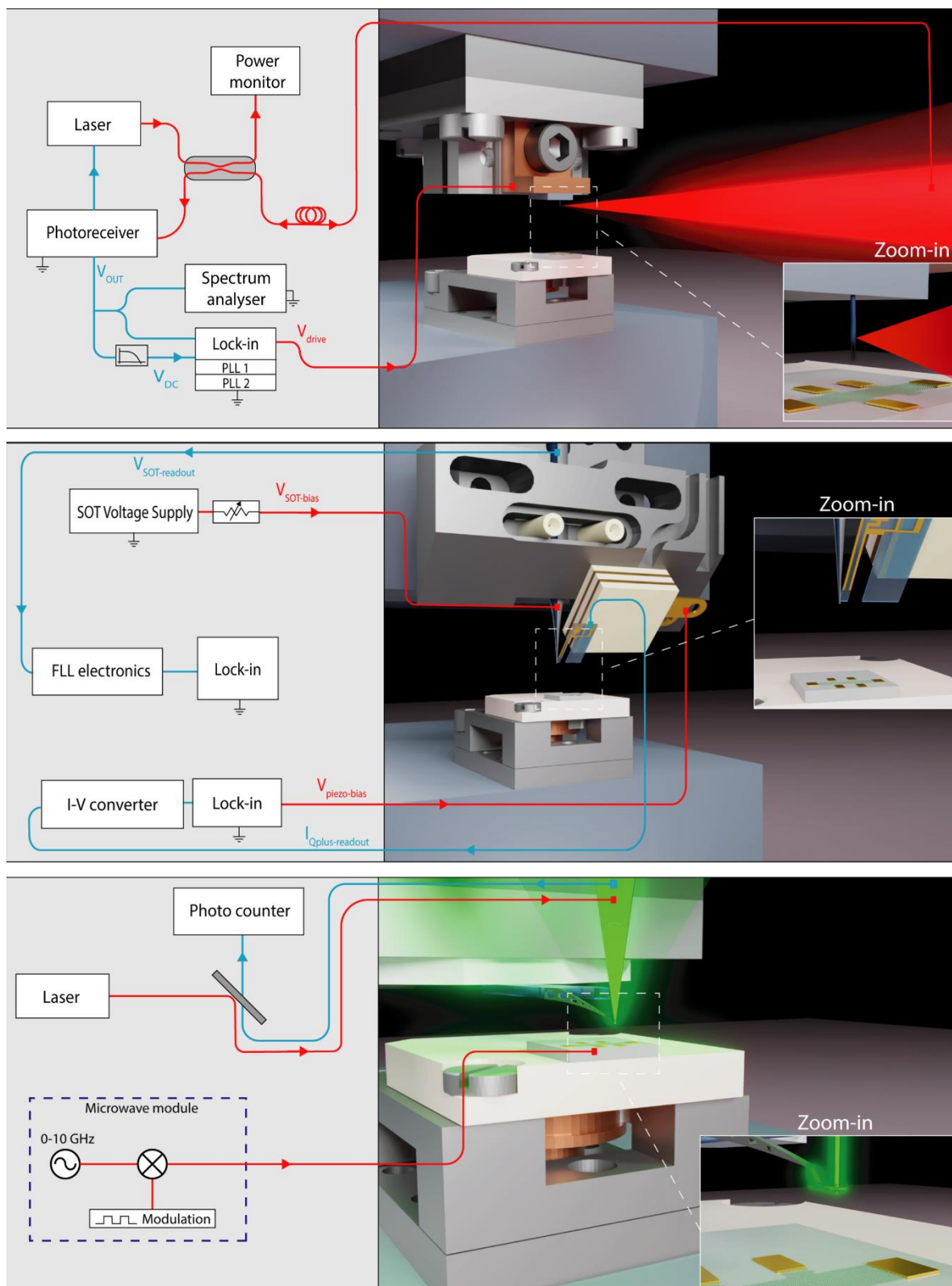
216 *Box 2: Magnetic field sources*

217 The magnetic field of a magnetic moment $\boldsymbol{m}$ at distance $\boldsymbol{r}$ is given by $\boldsymbol{B}_m = \frac{\mu_0}{4\pi r^3}\left(\frac{3\,(\boldsymbol{m}\cdot\boldsymbol{r})\boldsymbol{r}}{r^2} - \boldsymbol{m}\right)$ and

218 the magnetic field of a line of current $\boldsymbol{I}$ is given by: $\boldsymbol{B}_I = \frac{\mu_0 \boldsymbol{I}\times\boldsymbol{r}}{2\pi r^2}$, where μ_0 is the vacuum permeability.

219 Using these two equations, we can express the various quantities measured by our scanning probe
220 sensors as a function of tip-sample spacing in terms of μ_B of magnetic moment or A of current. For
221 example, for SNVM measuring the z-component of the stray magnetic field, the maximum measurable
222 signal from a single μ_B moment pointing along the z-direction at a tip-sample spacing z is $B_{\mu_B,z} =$

223 $\frac{\mu_0 \mu_B}{2\pi z^3}$, while the maximum from a line of current I flowing in the plane is $B_{I,z} = \frac{\mu_0 I}{4\pi z}$. Similar expressions

224 can be written for the maximum magnetic flux in the z-direction from the same moment and current

225 measured by SSM: $\Phi_{\mu_B,z} = \frac{\mu_0 \mu_B R^2}{2(z^2+R^2)^{3/2}}$, where R is the SQUID radius and $\Phi_{I,z} =$

226 $\frac{\mu_0 I D}{4\pi}\ln\left(\frac{D^2+4z^2+D\sqrt{D^2+4z^2}}{D^2+4z^2-D\sqrt{D^2+4z^2}}\right)$, where D is the length of one side of a square SQUID loop (to simplify the

227 calculation, the current is integrated over a square rather than a circular loop). The corresponding

228 maximum static magnetic field gradients measured by standard MFM are: $\frac{\partial B_{\mu_B,z}}{\partial z} = \frac{3\mu_0 \mu_B}{2\pi z^4}$ and $\frac{\partial B_{I,z}}{\partial z} =$

229 $\frac{3\sqrt{3}\mu_0 I}{16\pi z^2}$.

230 *Applications to 2D materials*
231 Despite the lack of conventional MFM studies on 2D materials, researchers are starting to employ
232 high-sensitivity MFM probes to visualize correlated states in 2D systems via frequency shift maps,
233 which can ultimately be reconstructed in current density or magnetization contrast. Such images
234 would be particularly useful for measuring the spatial localization of flowing currents, as in edge states,
235 and for the determination of length scales such as magnetic domain sizes and coherence lengths.
236 Visualizing current flow in MATBG [36] and WeT_2 [37,38] while they are electrostatically tuned into
237 their superconducting states, would help reveal the origin of this superconductivity and whether or
238 not it is topological. NW MFM may also help provide direct evidence for magnetism in 2D magnets or
239 even in the 2D semiconductor, monolayer MoS_2 [39,40]. Optical spectroscopy has provided evidence
240 of a high-field spin-polarized state in this material, however, confirmation of its presence via a direct
241 measurement of magnetic field has not yet been possible. NW MFM's high sensitivity and ability to
242 operate in high-field conditions make it promising for such an investigation.

243 MFM can also be used to map dissipation in a sample by measuring the power required to maintain a
244 constant oscillation amplitude. This type of contrast maps the energy transfer between the tip and
245 the sample and provides excellent contrast for nanometer-scale magnetic structure [41]. Since energy
246 dissipation plays a central role in the breakdown of topological protection, it may provide important
247 contrast in spatial studies of strongly correlated states in 2D vdW materials. Dissipation contrast has
248 been used to observe superconducting [42] and bulk structural phase transitions [43], as well as the
249 local density of states. 2D materials engineering allows for the fabrication of devices, in which a variety

250 of different physical phases can be accessed by the application of a gate voltage. Local measurements
251 of dissipation via MFM could be an important tool for making spatial maps of the transitions between
252 those states.

253
254 Figure 3: Representative schematic diagrams for the field-sensitive SPMs most applicable to 2D
255 systems for their combination of high spatial resolution and high magnetic field sensitivity. From top
256 to bottom these are NW MFM, SSM via SOT, and SNVM. In the bottom portion, each diagram shows

257   a sample mounted on a movable stage, actuated by piezoelectric positioners. For scale, the white
258   sample-holder in each diagram is 12 x 12 mm in lateral size. Above this sample, is the scanning probe
259   along with its corresponding readout scheme. Insets show zoomed-in views of each probe, which
260   more clearly depict the detection schemes. For NW MFM, in red, incident from the right, we see the
261   focused laser light used for interferometric detection of the NW's flexural motion. For the SSM, we
262   see the mechanically-coupled tuning fork used for tip-sample distance control. For the SNVM, in
263   green, incident from above, we see focused laser light for NV excitation.

264   ## Scanning SQUID microscopy

265   *Working principle and conditions*

266   Taking advantage of a SQUID's extreme sensitivity to magnetic flux, SSM was first realized in the early
267   1980s [44]. Contrast results from the magnetic flux threading through a superconducting loop that is
268   interrupted by at least one JJ. The SQUID's critical current is periodic in this flux – given by the magnetic
269   field integrated over the area of the loop $\Phi_z = \int \boldsymbol{B} \cdot \boldsymbol{dA}$ – with a period given by the flux quantum
270   Φ_0. By applying the appropriate current bias, one can detect voltages across the SQUID which
271   correspond to changes in magnetic field threading the SQUID loop corresponding to factions of a Φ_0,
272   typically down to 10^{-6} $\Phi_0/Hz^{1/2}$. For imaging applications, a DC SQUID with two JJs is most often used.
273   This loop – or a pick-up loop inductively coupled to it – is scanned above a target sample in order to
274   map the magnetic field profile. The loop's size is minimized in order to optimize spatial resolution.
275   SQUIDs operate only below a superconducting transition temperature, which is typically below 10 K,
276   but can be above the temperature of liquid nitrogen (77 K) for some high-T_c superconductors.

277   As shown in Fig. 3, an SSM system consists of the SQUID sensor or pick-up loop and piezoelectric
278   positioners for moving the sample. In high-sensitivity and high-resolution applications, these elements
279   are in a cryostat and in vacuum. Precise control of the sensor-sample distance can be achieved, for
280   example, by coupling it to a micromechanical tuning fork [45,46]. As in MFM, scan areas are in the
281   micrometer range and take several minutes. The SQUID sets the system's ultimate bandwidth, which
282   can be in the GHz range, however stray capacitance, cabling, and detection electronics typically limit
283   the bandwidth to tens of MHz or below.

284   As imaging resolution has improved from the micrometer- down into the nanometer-scale, a number
285   of strategies have been employed to realize ever-smaller sensors, which simultaneously retain high
286   magnetic flux sensitivity and can be scanned in close proximity to a sample. One strategy has involved
287   miniaturizing the pick-up loop of a conventional SQUID and placing it at the extreme corner of the chip
288   where it can come close to a sample. The most advanced of such devices use a loop with a 200-nm
289   inner diameter to achieve sub-micrometer imaging resolution and a sensitivity of 130 nT/Hz$^{1/2}$ [47].
290   Although this design has the advantage of allowing for susceptibility measurements, the size of the
291   sensor and minimum distance from the sample, which together determine the imaging resolution, are
292   limited by the complex fabrication process. In the last decade, this limitation has been addressed
293   through the development of SQUID-on-tip (SOT) sensors, consisting of a SQUID fabricated by shadow
294   evaporation or directional sputtering of a metallic superconductor directly on the end of a pulled
295   quartz tip [48,49]. This process has resulted in scanning SQUID sensors with diameters down to 50 nm,
296   100 nm imaging resolution, and a sensitivity of 5 nT/Hz$^{1/2}$ [50].

297   *Sensitivity to different types of contrast*

298   The noise limiting the measurement of magnetic flux in a SQUID arises from several sources including
299   Johnson noise, shot noise, 1/f noise, and quantum noise [24]. For SQUIDs smaller than 1 μm and at
300   frequencies high enough to avoid 1/f noise, quantum noise sets the fundamental limit on detectable
301   flux to be $\Phi_Q = (\hbar L)^{1/2}$, where $\hbar$ is Planck's constant and L is the loop inductance [24,51,52]. State-

302 of-the-art SOT sensors made from Pb combine the highest flux sensitivity with the smallest sensor
303 size. In the white-noise limit (measured in the kHz range), sensors with 50 nm diameter reach $\Phi_{min} =$
304 50 nΦ_0/Hz$^{1/2}$, which is about 4 times larger than Φ_Q [50]. Near DC (measured in the Hz range), where
305 the same sensor is limited by 1/f noise, Φ_{min} is about 10 times larger. In these devices, *L* is dominated
306 by kinetic rather than geometric inductance. For this reason, optimizing material parameters for low
307 kinetic inductance provides the best route for improving Φ_{min}.

308 What this sensitivity means in terms of magnetization or current sources requires knowing the tip-
309 sample spacing. Using the best 50-nm-diameter SOT at a spacing of 50 nm – closer approach than the
310 characteristic sensor size does not improve spatial resolution – the white noise level is equivalent to
311 the field of a few μ_B/Hz$^{1/2}$ or a few tens of nA/Hz$^{1/2}$, while at DC the device is ten times less sensitive.
312 Again, such estimates are shown as a function of probe-sample spacing in Figs. 4 a) and b).

313 *Applications to 2D materials*
314 SSM has already been successfully used to image current density via local measurements of Biot-
315 Savart fields. In particular, maps of the flow of equilibrium currents in graphene made using SOT
316 probes revealed the topological and non-topological components of edge currents in the quantum
317 Hall state [10]. The non-topological currents, which are of opposite polarity to the topological
318 currents, were predicted theoretically [53], but are not typically considered because they do not affect
319 conventional transport measurements [54]. In fact, although previous SPM experiments, including
320 Kelvin probe [55], scanning single-electron transistor [56], and scanning capacitance [57], revealed the
321 presence of compressible and incompressible regions, non-topological currents were never observed.
322 This new insight into the microscopic make-up of orbital currents in the quantum Hall systems was
323 made possible by the SSM's sensitivity to tiny magnetic fields. Similar images of equilibrium currents
324 in MATBG, revealed the twist-angle disorder in these samples with a resolution and over an extent
325 not possible by other techniques [8]. In those experiments, SSM also provided a direct correlation
326 between the degree of disorder and the presence of correlated states, including superconductivity. In
327 another set of measurements, SSM with the same kind of SOT sensor found evidence for orbital
328 magnetism in twisted bilayer graphene [9]. Images of the weak orbital magnetization and the
329 presence of micrometer-scale domains, both of which have not been previously observed, were –
330 once again – made possible by the technique's sensitivity to magnetic field combined with its spatial
331 resolution.

332 Given the SOT's exquisite sensitivity to local temperature, such probes can also be applied to measure
333 local sources of dissipation, as was demonstrated in experiments on graphene [58,59]. Similar
334 scanning probe measurements of magnetic field and dissipation could be carried out on other moiré
335 systems, including twisted transition metal dichalcogenides and twisted multi-layer graphene. These
336 systems are also predicted to host a variety of correlated states, including superconductivity, Mott
337 insulating states, magnetic states, and Wigner crystal states [60].

338 ## Scanning NV center microscopy
339 *Working principle and conditions*
340 Following proposals in 2008 pointing out its potential for high-resolution, high-sensitivity magnetic
341 field imaging [61,62], the last decade has seen a flurry of activity in the development of SNVM. In this
342 scheme, NV centers, which are optically addressable electronic defect spins in diamond, are used as
343 scanning single-spin sensors. Magnetic field measurements are carried out via optically-detected
344 magnetic resonance (ODMR) spectroscopy, where the EPR spectrum of the NV is recorded by
345 simultaneous microwave excitation and optical readout of the defect's spin state as the probe is
346 scanned in close proximity to the sample surface. Thanks to the technique of single-molecule

347 fluorescence, these experiments can be performed on a single spin [63]. The magnetic field sensitivity
348 results from a Zeeman shift of the spin resonances. In the regime of a weak orthogonal component of
349 an external magnetic field, the field component parallel to the NV symmetry axis leads to a linear shift
350 of the $m_s = \pm 1$ spin states with a proportionality given by the free-electron gyromagnetic ratio $\gamma =$
351 $2\pi \times 28$ GHz/T [64]. The ODMR spectrum is measured as a change in optical intensity as a function
352 of continuous-wave or pulsed microwave excitation [65]. Other forms of contrast include ODMR
353 quenching in magnetic fields larger than 10 mT due to energy-level mixing by the off-axis field
354 component [66,67] and spin relaxometry [83]. The latter probes high-frequency fluctuations near the
355 NV resonance (GHz range) and allows for the investigation of magnetic fluctuations and spin waves in
356 ferromagnets [68–70]. Further, dynamical decoupling techniques can be used to perform frequency
357 spectroscopy in the kHz-MHz range [71,72].

358 In scanning probe applications, as shown in Fig. 3, the NV center is hosted within a crystalline diamond
359 nanopillar and scanned over the sample of interest [61,73]. State-of-the-art diamond probes are
360 engineered with shallow NV centers, which are implanted at depths around 10 nm [74], in order to
361 minimize the distance between the NV center and the sample and thus to optimize both sensitivity
362 and spatial resolution. However, in most SNVM literature, the NV stand-off distance is 50 to 100 nm,
363 indicating that NV centers may be deeper than expected. As in MFM and SSM, the sample is scanned
364 below the probe, usually using piezoelectric positioners, while precise distance control is achieved by
365 coupling to a micromechanical tuning fork. An objective lens above the probe is used to optically excite
366 the NV center and to detect its fluorescence.

367 Using advanced sensing protocols and sequences of microwave and laser pulses, scanning NV center
368 microscopes have achieved field sensitivities down to a few µT/Hz$^{1/2}$ [75] for DC signals and around
369 100 nT/ Hz$^{1/2}$ [17] for AC signals. The best resolutions reported for scanning setups are between 15
370 and 25 nm [76,77], although resolution better than 10 nm should ultimately be possible for optimized
371 scanning tips with very shallow NV centers. On top of high sensitivity and spatial resolution, scanning
372 NV microscopy offers additional benefits: a large temperature range – including room temperature –
373 a quantitative measurement of the magnetic field that is intrinsically calibrated via natural constants,
374 vector sensitivity, and a number of spin manipulation protocols for performing spectroscopy from DC
375 to GHz signal frequencies.

376 These advantages notwithstanding, scanning NV microscopy remains challenging at high fields due to
377 the high microwave frequencies (10s to 100s of GHz) required to actuate the sensor electron spin, and
378 the spin-level mixing for magnetic fields that are not aligned with the NV symmetry axis [66,67].
379 Although NV center detection has been reported below 1 K, experiments at cryogenic temperatures
380 are hampered by reduced photoluminescence contrast and poor charge stability. Furthermore, the
381 required optical and microwave excitation sometimes poses a limit on the possible samples, since it
382 can perturb materials such as direct-band-gap semiconductors, nanomagnets, and fragile biological
383 structures.

384 *Sensitivity to different types of contrast*
385 SNVM is typically limited by photon shot noise from the optical readout, and can be expressed by a
386 simple signal-to-noise formula typical for optical magnetometry [78]. Specifically, the magnetic
387 sensitivity of the scanning NV magnetometer is determined by a combination of the spin dephasing
388 or decoherence time T_2, the optical contrast ϵ and the maximum photon count rate I_0. A generic
389 estimate for the minimum detectable magnetic field is given by $B_{\min} \approx \left[\gamma \epsilon \sqrt{I_0 t_{acq} T_2}\right]^{-1}$, where γ is
390 the gyromagnetic ratio and t_{acq} is the photon integration time. Using typical values ($\epsilon = 0.2$, $I_0 =$
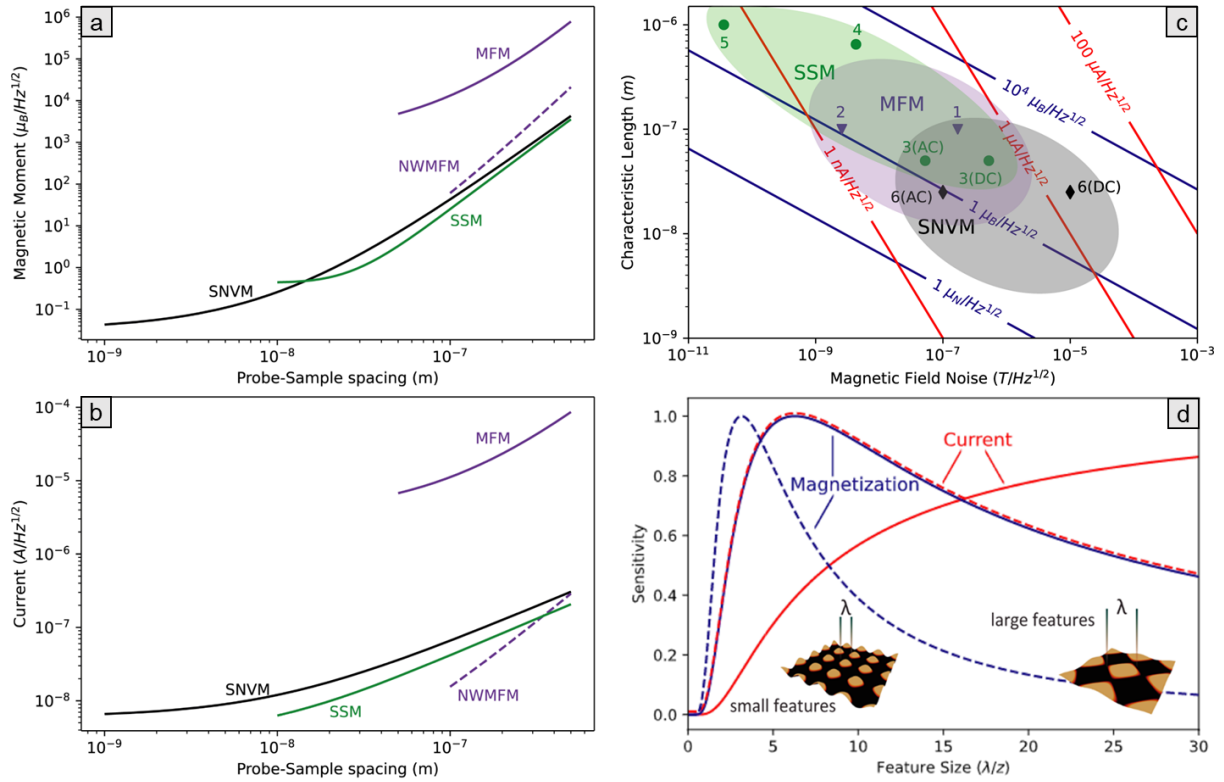391 200 kC/s, $t_{\mathrm{acq}} = 300$ ns, $T_2 = T_2^* = 1.5$ µs), the minimum detectable field is about 1 µT/Hz$^{1/2}$ for

392   pulsed operation and 10 μT/Hz$^{1/2}$ for continuous-wave operation. Recent SNVM experiments have
393   shown state-of-the-art pulsed sensitivity of 100 nT/Hz$^{1/2}$ [17]. In the future, the sensitivity can be
394   improved by extending T_2 using isotopically-purified (free of ^{13}C) material [79] and AC magnetometry
395   techniques [80], improving the contrast through alternative readout schemes [81], and improving the
396   count rate by photonic shaping [82,83].

397   If we assume the best demonstrated pulsed sensitivity and a 25 nm NV-sample distance, SNVM is
398   sensitive to one μ_B/Hz$^{1/2}$ or a few tens of nA/Hz$^{1/2}$. Fig. 2 shows such sensitivity estimates for some of
399   the best SNVM as a function of probe-sample spacing.

400   *Applications to 2D materials*
401   SNVM has been applied to image magnetization in the 2D ferromagnets [12–14] and current flow in
402   graphene [15,16,84] and layered semimetals [17]. Given SNVM's particularly high sensitivity to
403   magnetic moment, the technique is particularly suited for mapping magnetism in vdW magnets to
404   distinguish domain structure, quantify the strength of the magnetism, and confirm its origin. The
405   ability to distinguish the magnetism of single atomic layers, as first shown in CrI$_3$ [12] and later in
406   CrBr$_3$ [13] and CrTe$_2$ [14], is crucial for investigating the effect of each layer in vdW heterostructures.
407   The ability of SNVM to retain high sensitivity at room temperature and under ambient conditions
408   makes it applicable to magnetic systems with potential practical application in spintronic devices. Sub-
409   micrometer spatial resolution also distinguishes SNVM from optical techniques such a Kerr
410   effect [20,85] and magnetic circular dichroism microscopy [86,87], allowing it to resolve, for example,
411   domain walls pinned by defects [13]. Moreover, its ability to quantitatively measure stray field allows
412   the mapping of local 2D magnetization with a precision not possible via optical techniques. High-
413   frequency sensing with SNVM [88] may also be useful for investigating magnonic excitations in 2D
414   magnets.

415   Although current mapping at temperatures below 4 K, such as required for studies of
416   superconductivity in 2D materials, is still challenging, SNVM is ideal for experiments across a broad
417   and higher temperature range. In fact, researchers have used SNVM to map hydrodynamic flow in
418   graphene [15] and WTe$_2$ [17], which is strongest at intermediate temperatures. The ability to measure
419   current flow over a wide range of temperatures, allowed, in both of these systems, the observation of
420   a crossover from diffusive to viscous electron transport. In WTe$_2$, SNVM revealed as an unexpected
421   temperature dependence, indicating that strong electron-electron interactions are likely phonon-
422   mediated. Similar studies could be carried out in a plethora of other 2D systems, in which viscous
423   electron transport may dominate under certain conditions.

424

Figure 4: Comparing sensitivity and resolution. Plots comparing the sensitivity to magnetic moment (a) and current (b) of the 3 magnetic imaging techniques under the most favorable conditions, i.e. in vacuum and at liquid helium temperatures. We use parameters from van Schendel et al. for conventional MFM [34], Mattiat et al. for NW MFM [19], Vasyukov et al. for SSM [50], and Vool et al. for SNVM [17]. MFM and NW MFM sensitivities are based on frequency shift measurements at DC, while SNVM and SSM sensitivities are based on AC measurements usually in the tens of kHz range. (c) Plot showing the characteristic length and magnetic field noise of state-of-the-art scanning magnetic probes under ideal conditions, i.e. in vacuum and at liquid helium temperatures. The characteristic length sets the scale of the possible spatial resolution. Diagonal lines show the sensitivity required to measure the labelled magnetic moments and currents. Data points correspond to state-of-the-art SPMs demonstrated in the corresponding reference: 1, van Schendel et al. [34]; 2, Mattiat et al. [19]; 3, Vasyukov et al. [50]; 4, Kirtley et al. [24]; 5, Jeffery et al. [89]; 6, Vool et al. [17]. (d) Sensitivity as a function of feature size, expressed as the ratio between the feature's spatial wavelength λ and the probe-sample spacing z. (Solid lines) Magnetic field imaging is most sensitive to spatially large current features (red) and to magnetization features (blue) with a size similar to the probe-sample spacing z. (Dashed lines) Magnetic gradient imaging shifts the maximum sensitivity towards smaller feature size.

Comparison between techniques

Having quantified the sensitivity of MFM, SSM, and SNVM to magnetic moment and electrical current, we can now discern which techniques are best suited for mapping which type of contrast. Fig. 4 a) and b) show the sensitivity of all techniques to the magnetic field profile produced by a magnetic moment and a line of current as a function of probe-sample spacing. In the case of conventional and NW MFM, we refer to thermal limit of frequency shift measurements, which applies to DC or low-frequency measurements. In the other two cases, we use the minimum flux and field noise achieved in these devices in AC measurements in the tens of kHz range.

13

450

	MFM (conventional) [27,28,34,90]	MFM (NW) [19]	SSM (susceptometer) [47]	SSM (SOT) [50]	SNVM [17,75–77]
Sensor size	10-100 nm	100 nm	0.5 μm	50 nm	< 1 nm
Sensor stand-off	10-100 nm	50 nm	330 nm	25 nm	50 nm
Spatial resolution	10-100 nm	100 nm	0.5 μm	100 nm	15-25 nm
DC sensitivity	10-100 $\mu T/(Hz)^{1/2}$	3 $nT/(Hz)^{1/2}$	660 $nT/(Hz)^{1/2}$	50 $nT/(Hz)^{1/2}$	4 $\mu T/(Hz)^{1/2}$
AC sensitivity	170 $nT/(Hz)^{1/2}$	3 $nT/(Hz)^{1/2}$	130 $nT/(Hz)^{1/2}$	5 $nT/(Hz)^{1/2}$	100 $nT/(Hz)^{1/2}$
Operating field	< 10 T	< 10 T	< 30 mT	< 1.2 T	< 100s mT
Operating temp.	< 500 K	< 300 K	< 9 K	< 7 K	< 600 K

451 Table 1: Parameters for state-of-the-art magnetic SPM combining the highest-sensitivity with the
452 highest resolution, based on the devices discussed in the cited references. Values shown in gray
453 represent estimates based on the properties of the sensors, which have not yet been experimentally
454 confirmed.

455

456 Together with sensor size, probe-sample spacing sets the spatial resolution of an SPM technique.
457 Depending on the type of contrast, this spacing also strongly affects sensitivity. SSM sensitivity is not
458 shown closer than 10 nm, because sensors are difficult to operate closer without a catastrophic crash.
459 MFM sensitivity is not shown closer than 50 nm and NW MFM is not shown closer than 100 nm,
460 because the point-probe approximation breaks down at tip-sample spacings smaller than the tip size
461 and non-contact friction starts to dominate the force noise [91]. Also, at such close spacing, the stray
462 field produced by the MFM tip at the sample is often invasive. Since SNVM can essentially be operated
463 in contact with the sample, we plot its sensitivity down to 1 nm of probe-sample spacing.

464 Depending on tip-sample spacing, either SNVM or SSM have the highest sensitivity to magnetic
465 moment. SSM appears best for tip-sample distances larger than 25 nm, while SNVM is better for closer
466 approach. Conventional MFM is the least sensitive, while NW MFM is competitive with the other
467 techniques. While very promising, NW MFM tip size must be reduced from state-of-the-art diameters
468 of 100 nm in order for the technique to become competitive in high spatial resolution imaging of
469 magnetic moment.

470 Among proven techniques, SSM is most sensitive to current. While conventional MFM is the least
471 sensitive, NW MFM appears to surpass all techniques between 500 and 50 nm. Once again, for spatial
472 resolutions better than 10 nm SNVM appears to be the best choice.

473 Fig. 4 c) provides another way to compare the three techniques, by showing the characteristic length
474 of each sensor (its size in one dimension) together with its sensitivity to magnetic field. We plot a few

475 state-of-the-art sensors of each type and give an approximate idea of each technique's operating
476 regime. The characteristic length of a sensor not only sets its ultimate spatial resolution, but also sets
477 the optimum probe-sample spacing, since closer approach is either impossible or does not improve
478 sensitivity. Diagonal lines represent the combined probe-sample spacing and field noise required to
479 achieve a certain sensitivity to magnetic moment or current.

480 Fig. 4 c) makes clear that SNVM has the smallest characteristic length, due to the atomic-scale of the
481 NV center and the possibility to implant NVs with long coherence times just 10 nm from the surface
482 of a scanning probe. This makes SNVM the technique of choice for spatial resolution under 25 nm and
483 for the detection of small magnetizations. Because the magnetic field produced by a magnetic
484 moment drops of with the inverse cube of the probe-sample distance, a small sensor able to work in
485 close proximity to the sample is crucial for this type of contrast.

486 Fig. 4 c) also shows that SSM has the highest field sensitivity, but that it comes at the expense of large
487 sensor size. While conventional MFM appears too insensitive to measure weak magnetization or
488 current density, the increased force sensitivity of NW MFM makes it competitive with the other two
489 techniques. In fact, for the measurement of currents, where spatial resolutions better than 100 nm
490 are not required, SSM and NW MFM are the best techniques. Because Biot-Savart fields fall off only
491 with the inverse power of the probe-sample spacing, a small sensor is not as important in current
492 measurements as it is in magnetization measurements.

493 Aside from their sensitivity and resolution, each technique has properties making it more or less
494 advantageous for certain samples. The strongly magnetic tip of an MFM can produces tens of mT of
495 magnetic field on a sample 50 nm away. This field can in turn perturb the sample, potentially altering
496 its state. SNVM requires the excitation of the probe with visible laser light. This optical excitation can
497 perturb optically active samples below the probe. On the other hand, the stray fields due to the
498 Meissner effect on an SSM probe are nearly negligible, making these sensors minimally invasive. SSM,
499 however, is the most limited from the environmental point of view, functioning only at temperatures
500 below the superconducting transition of the SQUID, typically below 10 K. Both MFM and SNVM
501 function at a wide range of temperatures and pressures. SSM must also work below its critical field,
502 which for state-of-the-art SOTs can be as high as a few T. SNVM is also limited in field, in that the
503 frequency of the microwaves used to address the NV center scale linearly with field and become
504 impractically high above 1 T.

505

Reconstruction of magnetization or current from field images

507 Since magnetic field microscopy techniques do not directly image the current or magnetization
508 pattern, but rather their stray field, the question arises whether and how the former may be
509 reconstructed from a stray field map. The relation between stray field and current density is governed
510 by the Biot-Savart law that, via the concept of bound currents, can also be applied to magnetization.

511 Work in the late eighties by Roth [92] and Beardsley [93] established a framework to compute the
512 stray fields of two-dimensional current density J(x,y) and two-dimensional magnetization patterns
513 $M(x, y)$, respectively. The same work also specified the conditions, in which a reconstruction of J and
514 M is possible. In particular, they showed that three-dimensional current densities and magnetization
515 patterns do not produce a unique magnetic stray field pattern, and can therefore not be determined
516 by stray field imaging. Further, even an arbitrary two-dimensional magnetization pattern does not
517 possess a unique stray field because the divergence-free part of M does not generate an external
518 stray field and is left arbitrary [93]. A rigorous solution, on the other hand, exists for two-dimensional

519   current densities $\boldsymbol{J} = (J_x, J_y, 0)$ and out-of-plane magnetized films $\boldsymbol{M} = (0,0, M_z)$. It has further been
520   shown that this solution can be extended to thick films if the magnetization, or current density, is
521   uniform through the thickness [76]. As a consequence, magnetic field imaging is especially useful for
522   analyzing 2D systems and thin-film devices.

523   Magnetic field maps do not reproduce all current or magnetization features with the same sensitivity.
524   Looking at the mechanics of the reconstruction, shown in Box 3, it becomes clear that features smaller
525   than the probe-sample spacing z produce negligible magnetic field at the sensor location, because
526   stray fields decay exponentially with distance from the surface. The decay length is given by $\lambda/2\pi$,
527   where λ is the spatial wavelength of the current or magnetization feature, as shown in Fig. 4 d).
528   Interestingly, large features compared to the probe-sample spacing, i.e. large λ/z, produce a strong
529   signal for currents, but not for magnetization.

530   Imaging magnetic field gradients rather than magnetic fields, allows one to push the maximum
531   sensitivity towards smaller feature size. Magnetic gradient detection is the standard mode for MFM,
532   but can also be implemented for SSM and SNVM by a mechanical oscillation of the sensor [10,61].
533   Using lock-in techniques to demodulate the resulting signal can also significantly reduce noise through
534   spectral filtering. Gradient detection is especially attractive for imaging currents, because the
535   magnetic gradient image closely resembles the current density image, so that no reconstruction is
536   needed [10]. For SNVM, gradient imaging is attractive because it upconverts DC signals to AC where
537   much more sensitive magnetometry protocols are available [61,80].

538   *Box 3: Reconstruction of current density and magnetization from a magnetic field image*
539   The current density $\boldsymbol{J} = (J_x, J_y)$ and in-plane magnetization M_z of a two-dimensional sample can be
540   conveniently reconstructed from a magnetic field image by expressing the Biot-Savart law in k-space.
541   Assume that we image in a plane at distance z above the sample, the magnetic stray field, in k-space
542   is given by: $B_z(k_x, k_y, z) = ig(k,z)[\frac{k_y}{k} J_x(k_x, k_y) - \frac{k_x}{k} J_y(k_x, k_y)]$, where $g(k,z) = \frac{1}{2}\mu_0 d e^{-kz}$ is a
543   transfer function with $d \ll z$ being the film thickness, k_x and k_y are the k-vectors, and $k = $
544    $\left(k_x^2 + k_y^2\right)^{1/2}$. Similar expressions can be derived for B_x and B_y as well as for $d \geq z$ [76,92]. To
545   reconstruct the current density from a magnetic field map, the relation is inverted: $J_x(k_x, k_y) = $
546    $-\frac{ik_y W B_z(k_x, k_y, z)}{kg(k,z)}$ and $J_y(k_x, k_y) = -\frac{ik_x W B_z(k_x, k_y, z)}{kg(k,z)}$, where W is a window function, whose cut-off
547   wavelength is adjusted to suppress high-frequency noise. Different choices for the window function
548   have been reported in the literature, including Hann and rectangular and Tikhonov-based windows.
549   The cut-off wavelength typically is of order z. An expression for reconstructing $\boldsymbol{J}$ from an arbitrary B-
550   field component is given in [76].

551   Similar expressions can be derived for reconstructing an out-of-plane magnetization M_z or to
552   reconstruct magnetic gradient images. To reconstruct M_z, note that $\boldsymbol{J} = \nabla \times \boldsymbol{M}$, and therefore:
553    $B_z(k_x, k_y) = kg(k,z)M_z(k_x, k_y)$ for the forward problem as well as $M_z(k_x, k_y) = \frac{W B_z(k_x, k_y, z)}{kg(z,k)}$ for the
554   reverse problem. To reconstruct a magnetic gradient image, the transfer function incurs an additional
555   factor of k due to the derivative.

556

Prospects for improvement

558   Improving MFM sensitivity requires stronger magnetic tips or transducers with better force sensitivity.
559   Up to an order of magnitude in force sensitivity could be gained by using optimized NW transducers.
560   MFM cantilevers have recently been realized with spring constants in the hundreds of mN/m and

561 mechanical quality factors above 10^6, resulting in nearly 100 times more sensitivity than conventional
562 transducers. In general, however, improving the sensitivity of a mechanical transducer is achieved by
563 reducing its size [94], as in recent work on NW MFM. Another route to improve magnetic field
564 sensitivity is to increase the magnetic moment and size of MFM tips. This gain, however, comes at the
565 cost of reducing spatial resolution and increasing the perturbative effect of the probes, which now
566 produce larger stray fields at the sample.

567 The spatial resolution of the MFM could be improved by utilizing the sharpest possible magnetic tips.
568 Extensive work has been done in this area in the context of conventional MFM, achieving spatial
569 resolutions down to 10 nm [95–98]. Such work could be extended to high-force-sensitivity NW MFM.
570 Smaller tips, however, have reduced magnetic moment and, consequently, a worse sensitivity to
571 magnetic field profiles. In order to maintain high sensitivity, in general, the reduction in tip size should
572 be accompanied with a reduction in transducer size.

573 Improvements in SSM field sensitivity could come from a reduction in the SQUID inductance. Given
574 that this quantity is dominated by kinetic inductance in state-of-the-art devices, optimizing the
575 superconducting material from which the device is made could be a fruitful pursuit. Further reduction
576 of the characteristic size of SSM probes is difficult to imagine. SOT probes have been fabricated with
577 diameters just under 50 nm. Reducing this size further would make the device size similar to the
578 thickness of the deposited superconducting film, complicating much of the process, on which the
579 fabrication is based. SQUIDs with feature sizes of only a few nanometers have been fabricated in YBCO
580 using a focused ion beam of He [99], raising the possibility of devices that are an order of magnitude
581 smaller and potentially work at liquid nitrogen temperature. Nevertheless, significant work remains
582 to be done before such devices can be integrated onto scanning probes.

583 In order to reduce the characteristic length scale of SNVM, a number of researchers have focused on
584 simultaneously reducing the implantation depth of NV centers and maintaining their coherence
585 properties. Implantation depths of less than 3 nm have been reported combined with greater than 10
586 μs coherence times [100], giving a perspective of better than 10 nm imaging resolution combined with
587 sub-10 $nT/Hz^{1/2}$ sensitivity. So far, however, most reported stand-off distances remain between 50
588 and 100 nm and the best magnetic field sensitivities at 100 $nT/Hz^{1/2}$ and significant work may be
589 needed to reduce either figure of merit.

590

Conclusion

592 The confluence of substantial improvements in nanometer-scale magnetic imaging with the advent of
593 engineered 2D materials creates the perfect opportunity to gain new insight into the physics of
594 correlated states in condensed matter. The unprecedented control provided by layer-by-layer
595 material engineering gives physicists a vast playground on which to test theories on superconductivity,
596 magnetism, and other correlated phenomena. With this control, however, comes sensitivity to
597 disorder and inhomogeneity. In such a fragile environment, local measurements – with sensors whose
598 characteristic size is smaller than the length scale of the disorder – are essential for making sense of
599 the system. For this reason, SPM techniques will become ever more important tools in this growing
600 field, perhaps only losing traction, once fabrication techniques have been honed and substantially
601 improved.

602 There are a number of SPM techniques, which have emerged as important tools for the investigation
603 of 2D systems. Conventional atomic force microscopy has been used extensively for topographic
604 characterization of 2D materials. In graphene, scanning single electron transistors have been used to

map the local density of states [101] and for imaging hydrodynamic flow [102]. Scanning gate microscopy has been used to image localized states [103] and scanning microwave impedance microscopy for visualizing the structural details of moiré lattices [104]. Electronic properties of 2D transition metal dichalcogenides have also been studied by scanning tunnelling microscopy [105]. Scanning near-field optical microscopy has even been used to measure polaritonic response in graphene-hexagonal boron nitride heterostructures [106].

As discussed in this review, among these SPM techniques, those involving non-invasive magnetic field imaging are particularly suited to investigating the correlated states present in 2D systems, because of their ability to map both current and out-of-plane magnetization. Given the high sensitivity and spatial resolution required to investigate correlated states in 2D materials, it is important to choose the appropriate magnetic SPM for the physical system under investigation. The different scaling of magnetization and current contrast with probe-sample spacing and the different physical quantities that are measured by various magnetic SPM make certain techniques more amenable to certain systems. We hope to have provided some insight in this regard, both to experimentalists wanting to apply magnetic SPM to 2D systems and to physicists working on the next generation of magnetic imaging techniques.

Acknowledgements

References:

[1]   K. S. Novoselov, A. K. Geim, S. V. Morozov, D. Jiang, Y. Zhang, S. V. Dubonos, I. V. Grigorieva, and A. A. Firsov, *Electric Field Effect in Atomically Thin Carbon Films*, Science **306**, 666 (2004).

[2]   M. R. Freeman and B. C. Choi, *Advances in Magnetic Microscopy*, Science **294**, 1484 (2001).

[3]   J. McCord, *Progress in Magnetic Domain Observation by Advanced Magneto-Optical Microscopy*, J. Phys. D: Appl. Phys. **48**, 333001 (2015).

[4]   N. Rougemaille and A. K. Schmid, *Magnetic Imaging with Spin-Polarized Low-Energy Electron Microscopy*, Eur. Phys. J. Appl. Phys. **50**, 2 (2010).

[5]   H. Stoll, M. Noske, M. Weigand, K. Richter, B. Krüger, R. M. Reeve, M. Hänze, C. F. Adolff, F.-U. Stein, G. Meier, M. Kläui, and G. Schütz, *Imaging Spin Dynamics on the Nanoscale Using X-Ray Microscopy*, Front. Phys. **3**, (2015).

[6]   S. Bonetti, *X-Ray Imaging of Spin Currents and Magnetisation Dynamics at the Nanoscale*, J. Phys.: Condens. Matter **29**, 133004 (2017).

[7]   P. Fischer, *Magnetic Imaging with Polarized Soft X-Rays*, J. Phys. D: Appl. Phys. **50**, 313002 (2017).

[8]   A. Uri, S. Grover, Y. Cao, J. A. Crosse, K. Bagani, D. Rodan-Legrain, Y. Myasoedov, K. Watanabe, T. Taniguchi, P. Moon, M. Koshino, P. Jarillo-Herrero, and E. Zeldov, *Mapping the Twist-Angle Disorder and Landau Levels in Magic-Angle Graphene*, Nature **581**, 7806 (2020).

[9]   C. L. Tschirhart, M. Serlin, H. Polshyn, A. Shragai, Z. Xia, J. Zhu, Y. Zhang, K. Watanabe, T. Taniguchi, M. E. Huber, and A. F. Young, *Imaging Orbital Ferromagnetism in a Moir\'e Chern Insulator*, ArXiv:2006.08053 [Cond-Mat] (2020).

651 [10] A. Uri, Y. Kim, K. Bagani, C. K. Lewandowski, S. Grover, N. Auerbach, E. O. Lachman, Y.
652   Myasoedov, T. Taniguchi, K. Watanabe, J. Smet, and E. Zeldov, *Nanoscale Imaging of*
653   *Equilibrium Quantum Hall Edge Currents and of the Magnetic Monopole Response in*
654   *Graphene*, Nature Physics **16**, 2 (2020).
655 [11] A. Aharon-Steinberg, A. Marguerite, D. J. Perello, K. Bagani, T. Holder, Y. Myasoedov, L. S.
656   Levitov, A. K. Geim, and E. Zeldov, *Long-Range Nontopological Edge Currents in Charge-*
657   *Neutral Graphene*, ArXiv:2012.02842 [Cond-Mat] (2020).
658 [12] L. Thiel, Z. Wang, M. A. Tschudin, D. Rohner, I. Gutiérrez-Lezama, N. Ubrig, M. Gibertini, E.
659   Giannini, A. F. Morpurgo, and P. Maletinsky, *Probing Magnetism in 2D Materials at the*
660   *Nanoscale with Single-Spin Microscopy*, Science **364**, 973 (2019).
661 [13] Q.-C. Sun, T. Song, E. Anderson, T. Shalomayeva, J. Förster, A. Brunner, T. Taniguchi, K.
662   Watanabe, J. Gräfe, R. Stöhr, X. Xu, and J. Wrachtrup, *Magnetic Domains and Domain Wall*
663   *Pinning in Two-Dimensional Ferromagnets Revealed by Nanoscale Imaging*, ArXiv:2009.13440
664   [Cond-Mat, Physics:Quant-Ph] (2020).
665 [14] F. Fabre, A. Finco, A. Purbawati, A. Hadj-Azzem, N. Rougemaille, J. Coraux, I. Philip, and V.
666   Jacques, *Characterization of Room-Temperature in-Plane Magnetization in Thin Flakes of*
667   *CrTe\$_2\$ with a Single Spin Magnetometer*, ArXiv:2011.05722 [Cond-Mat] (2021).
668 [15] A. Jenkins, S. Baumann, H. Zhou, S. A. Meynell, D. Yang, K. Watanabe, T. Taniguchi, A. Lucas,
669   A. F. Young, and A. C. B. Jayich, *Imaging the Breakdown of Ohmic Transport in Graphene*,
670   ArXiv:2002.05065 [Cond-Mat] (2020).
671 [16] M. J. H. Ku, T. X. Zhou, Q. Li, Y. J. Shin, J. K. Shi, C. Burch, L. E. Anderson, A. T. Pierce, Y. Xie, A.
672   Hamo, U. Vool, H. Zhang, F. Casola, T. Taniguchi, K. Watanabe, M. M. Fogler, P. Kim, A.
673   Yacoby, and R. L. Walsworth, *Imaging Viscous Flow of the Dirac Fluid in Graphene*, Nature
674   **583**, 7817 (2020).
675 [17] U. Vool, A. Hamo, G. Varnavides, Y. Wang, T. X. Zhou, N. Kumar, Y. Dovzhenko, Z. Qiu, C. A. C.
676   Garcia, A. T. Pierce, J. Gooth, P. Anikeeva, C. Felser, P. Narang, and A. Yacoby, *Imaging*
677   *Phonon-Mediated Hydrodynamic Flow in WTe2 with Cryogenic Quantum Magnetometry*,
678   ArXiv:2009.04477 [Cond-Mat, Physics:Quant-Ph] (2020).
679 [18] N. Rossi, B. Gross, F. Dirnberger, D. Bougeard, and M. Poggio, *Magnetic Force Sensing Using a*
680   *Self-Assembled Nanowire*, Nano Lett. **19**, 930 (2019).
681 [19] H. Mattiat, N. Rossi, B. Gross, J. Pablo-Navarro, C. Magén, R. Badea, J. Berezovsky, J. M. De
682   Teresa, and M. Poggio, *Nanowire Magnetic Force Sensors Fabricated by Focused-Electron-*
683   *Beam-Induced Deposition*, Phys. Rev. Applied **13**, 044043 (2020).
684 [20] B. Huang, G. Clark, E. Navarro-Moratalla, D. R. Klein, R. Cheng, K. L. Seyler, D. Zhong, E.
685   Schmidgall, M. A. McGuire, D. H. Cobden, W. Yao, D. Xiao, P. Jarillo-Herrero, and X. Xu, *Layer-*
686   *Dependent Ferromagnetism in a van Der Waals Crystal down to the Monolayer Limit*, Nature
687   **546**, 7657 (2017).
688 [21] W. Chen, Z. Sun, Z. Wang, L. Gu, X. Xu, S. Wu, and C. Gao, *Direct Observation of van Der Waals*
689   *Stacking–Dependent Interlayer Magnetism*, Science **366**, 983 (2019).
690 [22] J. Girovsky, M. Buzzi, C. Wäckerlin, D. Siewert, J. Nowakowski, P. M. Oppeneer, F. Nolting, T.
691   A. Jung, A. Kleibert, and N. Ballav, *Investigating Magneto-Chemical Interactions at Molecule–*
692   *Substrate Interfaces by X-Ray Photo-Emission Electron Microscopy*, Chem. Commun. **50**, 5190
693   (2014).
694 [23] B. Huang, M. A. McGuire, A. F. May, D. Xiao, P. Jarillo-Herrero, and X. Xu, *Emergent*
695   *Phenomena and Proximity Effects in Two-Dimensional Magnets and Heterostructures*, Nature
696   Materials **19**, 12 (2020).
697 [24] J. R. Kirtley, *Fundamental Studies of Superconductors Using Scanning Magnetic Imaging*, Rep.
698   Prog. Phys. **73**, 126501 (2010).
699 [25] Y. Martin and H. K. Wickramasinghe, *Magnetic Imaging by '"Force Microscopy"' with 1000 Å*
700   *Resolution*, Applied Physics Letters **50**, 1455 (1987).

[26] J. J. Sáenz, N. García, P. Grütter, E. Meyer, H. Heinzelmann, R. Wiesendanger, L. Rosenthaler, H. R. Hidber, and H. -J. Güntherodt, *Observation of Magnetic Forces by the Atomic Force Microscope*, Journal of Applied Physics **62**, 4293 (1987).

[27] I. Schmid, M. A. Marioni, P. Kappenberger, S. Romer, M. Parlinska-Wojtan, H. J. Hug, O. Hellwig, M. J. Carey, and E. E. Fullerton, *Exchange Bias and Domain Evolution at 10 Nm Scales*, Phys. Rev. Lett. **105**, 197201 (2010).

[28] A. Moser, M. Xiao, P. Kappenberger, K. Takano, W. Weresin, Y. Ikeda, H. Do, and H. J. Hug, *High-Resolution Magnetic Force Microscopy Study of High-Density Transitions in Perpendicular Recording Media*, Journal of Magnetism and Magnetic Materials **287**, 298 (2005).

[29] N. Rossi, F. R. Braakman, D. Cadeddu, D. Vasyukov, G. Tütüncüoglu, A. Fontcuberta i Morral, and M. Poggio, *Vectorial Scanning Force Microscopy Using a Nanowire Sensor*, Nat Nano **12**, 150 (2017).

[30] L. M. de Lépinay, B. Pigeau, B. Besga, P. Vincent, P. Poncharal, and O. Arcizet, *A Universal and Ultrasensitive Vectorial Nanomechanical Sensor for Imaging 2D Force Fields*, Nat Nano **12**, 156 (2017).

[31] A. Siria and A. Niguès, *Electron Beam Detection of a Nanotube Scanning Force Microscope*, Scientific Reports **7**, 11595 (2017).

[32] M. Poggio, *Nanomechanics: Sensing from the Bottom Up*, Nature Nanotechnology **8**, 482 (2013).

[33] J. M. Nichol, E. R. Hemesath, L. J. Lauhon, and R. Budakian, *Nanomechanical Detection of Nuclear Magnetic Resonance Using a Silicon Nanowire Oscillator*, Phys. Rev. B **85**, 054414 (2012).

[34] P. J. A. van Schendel, H. J. Hug, B. Stiefel, S. Martin, and H.-J. Güntherodt, *A Method for the Calibration of Magnetic Force Microscopy Tips*, Journal of Applied Physics **88**, 435 (2000).

[35] M. Sansa, E. Sage, E. C. Bullard, M. Gély, T. Alava, E. Colinet, A. K. Naik, L. G. Villanueva, L. Duraffourg, M. L. Roukes, G. Jourdan, and S. Hentz, *Frequency Fluctuations in Silicon Nanoresonators*, Nat Nano **11**, 552 (2016).

[36] Y. Cao, V. Fatemi, S. Fang, K. Watanabe, T. Taniguchi, E. Kaxiras, and P. Jarillo-Herrero, *Unconventional Superconductivity in Magic-Angle Graphene Superlattices*, Nature (2018).

[37] V. Fatemi, S. Wu, Y. Cao, L. Bretheau, Q. D. Gibson, K. Watanabe, T. Taniguchi, R. J. Cava, and P. Jarillo-Herrero, *Electrically Tunable Low-Density Superconductivity in a Monolayer Topological Insulator*, Science **362**, 926 (2018).

[38] E. Sajadi, T. Palomaki, Z. Fei, W. Zhao, P. Bement, C. Olsen, S. Luescher, X. Xu, J. A. Folk, and D. H. Cobden, *Gate-Induced Superconductivity in a Monolayer Topological Insulator*, Science **362**, 922 (2018).

[39] J. G. Roch, G. Froehlicher, N. Leisgang, P. Makk, K. Watanabe, T. Taniguchi, and R. J. Warburton, *Spin-Polarized Electrons in Monolayer MoS 2*, Nature Nanotechnology **14**, 432 (2019).

[40] J. G. Roch, D. Miserev, G. Froehlicher, N. Leisgang, L. Sponfeldner, K. Watanabe, T. Taniguchi, J. Klinovaja, D. Loss, and R. J. Warburton, *First-Order Magnetic Phase Transition of Mobile Electrons in Monolayer ${\mathrm{MoS}}_{2}$*, Phys. Rev. Lett. **124**, 187602 (2020).

[41] P. Grütter, Y. Liu, P. LeBlanc, and U. Dürig, *Magnetic Dissipation Force Microscopy*, Appl. Phys. Lett. **71**, 279 (1997).

[42] M. Kisiel, E. Gnecco, U. Gysin, L. Marot, S. Rast, and E. Meyer, *Suppression of Electronic Friction on Nb Films in the Superconducting State*, Nature Materials **10**, 119 (2011).

[43] M. Kisiel, F. Pellegrini, G. E. Santoro, M. Samadashvili, R. Pawlak, A. Benassi, U. Gysin, R. Buzio, A. Gerbi, E. Meyer, and E. Tosatti, *Noncontact Atomic Force Microscope Dissipation Reveals a Central Peak of ${\mathrm{SrTiO}}_{3}$ Structural Phase Transition*, Phys. Rev. Lett. **115**, 046101 (2015).

751   [44]   F. P. Rogers, *A Device for Experimental Observation of Flux Vortices Trapped in*
752   *Superconducting Thin Films*, Thesis, Massachusetts Institute of Technology, 1983.
753   [45]   A. Finkler, D. Vasyukov, Y. Segev, L. Ne'eman, E. O. Lachman, M. L. Rappaport, Y. Myasoedov,
754   E. Zeldov, and M. E. Huber, *Scanning Superconducting Quantum Interference Device on a Tip*
755   *for Magnetic Imaging of Nanoscale Phenomena*, Review of Scientific Instruments **83**, 073702
756   (2012).
757   [46]   L. Ceccarelli, Scanning Probe Microscopy with SQUID-on-Tip Sensor, Thesis,
758   University_of_Basel, 2020.
759   [47]   J. R. Kirtley, L. Paulius, A. J. Rosenberg, J. C. Palmstrom, C. M. Holland, E. M. Spanton, D.
760   Schiessl, C. L. Jermain, J. Gibbons, Y.-K.-K. Fung, M. E. Huber, D. C. Ralph, M. B. Ketchen, G. W.
761   Gibson, and K. A. Moler, *Scanning SQUID Susceptometers with Sub-Micron Spatial Resolution*,
762   Review of Scientific Instruments **87**, 093702 (2016).
763   [48]   A. Finkler, Y. Segev, Y. Myasoedov, M. L. Rappaport, L. Ne'eman, D. Vasyukov, E. Zeldov, M. E.
764   Huber, J. Martin, and A. Yacoby, *Self-Aligned Nanoscale SQUID on a Tip*, Nano Lett. **10**, 1046
765   (2010).
766   [49]   K. Bagani, J. Sarkar, A. Uri, M. L. Rappaport, M. E. Huber, E. Zeldov, and Y. Myasoedov,
767   *Sputtered Mo66Re34 SQUID-on-Tip for High-Field Magnetic and Thermal Nanoimaging*, Phys.
768   Rev. Applied **12**, 044062 (2019).
769   [50]   D. Vasyukov, Y. Anahory, L. Embon, D. Halbertal, J. Cuppens, L. Neeman, A. Finkler, Y. Segev,
770   Y. Myasoedov, M. L. Rappaport, M. E. Huber, and E. Zeldov, *A Scanning Superconducting*
771   *Quantum Interference Device with Single Electron Spin Sensitivity*, Nat Nano **8**, 639 (2013).
772   [51]   C. D. Tesche and J. Clarke, *Dc SQUID: Noise and Optimization*, Journal of Low Temperature
773   Physics **29**, 301 (1977).
774   [52]   M. W. Mitchell and S. Palacios Alvarez, *Colloquium: Quantum Limits to the Energy Resolution*
775   *of Magnetic Field Sensors*, Rev. Mod. Phys. **92**, 021001 (2020).
776   [53]   M. R. Geller and G. Vignale, *Currents in the Compressible and Incompressible Regions of the*
777   *Two-Dimensional Electron Gas*, Phys. Rev. B **50**, 11714 (1994).
778   [54]   N. R. Cooper, B. I. Halperin, and I. M. Ruzin, *Thermoelectric Response of an Interacting Two-*
779   *Dimensional Electron Gas in a Quantizing Magnetic Field*, Phys. Rev. B **55**, 2344 (1997).
780   [55]   Weis J. and von Klitzing K., *Metrology and Microscopic Picture of the Integer Quantum Hall*
781   *Effect*, Philosophical Transactions of the Royal Society A: Mathematical, Physical and
782   Engineering Sciences **369**, 3954 (2011).
783   [56]   B. E. Feldman, B. Krauss, J. H. Smet, and A. Yacoby, *Unconventional Sequence of Fractional*
784   *Quantum Hall States in Suspended Graphene*, Science **337**, 1196 (2012).
785   [57]   M. E. Suddards, A. Baumgartner, M. Henini, and C. J. Mellor, *Scanning Capacitance Imaging of*
786   *Compressible and Incompressible Quantum Hall Effect Edge Strips*, New J. Phys. **14**, 083015
787   (2012).
788   [58]   D. Halbertal, J. Cuppens, M. B. Shalom, L. Embon, N. Shadmi, Y. Anahory, H. R. Naren, J.
789   Sarkar, A. Uri, Y. Ronen, Y. Myasoedov, L. S. Levitov, E. Joselevich, A. K. Geim, and E. Zeldov,
790   *Nanoscale Thermal Imaging of Dissipation in Quantum Systems*, Nature **539**, 407 (2016).
791   [59]   D. Halbertal, M. B. Shalom, A. Uri, K. Bagani, A. Y. Meltzer, I. Marcus, Y. Myasoedov, J.
792   Birkbeck, L. S. Levitov, A. K. Geim, and E. Zeldov, *Imaging Resonant Dissipation from Individual*
793   *Atomic Defects in Graphene*, Science **358**, 1303 (2017).
794   [60]   E. Y. Andrei, D. K. Efetov, P. Jarillo-Herrero, A. H. MacDonald, K. F. Mak, T. Senthil, E. Tutuc, A.
795   Yazdani, and A. F. Young, *The Marvels of Moiré Materials*, Nature Reviews Materials 1 (2021).
796   [61]   C. L. Degen, *Scanning Magnetic Field Microscope with a Diamond Single-Spin Sensor*, Applied
797   Physics Letters **92**, 243111 (2008).
798   [62]   G. Balasubramanian, I. Y. Chan, R. Kolesov, M. Al-Hmoud, J. Tisler, C. Shin, C. Kim, A. Wojcik,
799   P. R. Hemmer, A. Krueger, T. Hanke, A. Leitenstorfer, R. Bratschitsch, F. Jelezko, and J.
800   Wrachtrup, *Nanoscale Imaging Magnetometry with Diamond Spins under Ambient*
801   *Conditions*, Nature **455**, 648 (2008).

[63] A. Gruber, A. Dräbenstedt, C. Tietz, L. Fleury, J. Wrachtrup, and C. von Borczyskowski, *Scanning Confocal Optical Microscopy and Magnetic Resonance on Single Defect Centers*, Science **276**, 2012 (1997).

[64] S. Felton, A. M. Edmonds, M. E. Newton, P. M. Martineau, D. Fisher, D. J. Twitchen, and J. M. Baker, *Hyperfine Interaction in the Ground State of the Negatively Charged Nitrogen Vacancy Center in Diamond*, Phys. Rev. B **79**, 075203 (2009).

[65] R. Schirhagl, K. Chang, M. Loretz, and C. L. Degen, *Nitrogen-Vacancy Centers in Diamond: Nanoscale Sensors for Physics and Biology*, Annu. Rev. Phys. Chem. **65**, 83 (2014).

[66] R. J. Epstein, F. M. Mendoza, Y. K. Kato, and D. D. Awschalom, *Anisotropic Interactions of a Single Spin and Dark-Spin Spectroscopy in Diamond*, Nature Physics **1**, 2 (2005).

[67] J.-P. Tetienne, L. Rondin, P. Spinicelli, M. Chipaux, T. Debuisschert, J.-F. Roch, and V. Jacques, *Magnetic-Field-Dependent Photodynamics of Single NV Defects in Diamond: An Application to Qualitative All-Optical Magnetic Imaging*, New J. Phys. **14**, 103033 (2012).

[68] C. S. Wolfe, V. P. Bhallamudi, H. L. Wang, C. H. Du, S. Manuilov, R. M. Teeling-Smith, A. J. Berger, R. Adur, F. Y. Yang, and P. C. Hammel, *Off-Resonant Manipulation of Spins in Diamond via Precessing Magnetization of a Proximal Ferromagnet*, Phys. Rev. B **89**, 180406 (2014).

[69] T. van der Sar, F. Casola, R. Walsworth, and A. Yacoby, *Nanometre-Scale Probing of Spin Waves Using Single Electron Spins*, Nature Communications **6**, 1 (2015).

[70] I. Bertelli, J. J. Carmiggelt, T. Yu, B. G. Simon, C. C. Pothoven, G. E. W. Bauer, Y. M. Blanter, J. Aarts, and T. van der Sar, *Magnetic Resonance Imaging of Spin-Wave Transport and Interference in a Magnetic Insulator*, Science Advances **6**, eabd3556 (2020).

[71] G. A. Álvarez and D. Suter, *Measuring the Spectrum of Colored Noise by Dynamical Decoupling*, Phys. Rev. Lett. **107**, 230501 (2011).

[72] C. L. Degen, F. Reinhard, and P. Cappellaro, *Quantum Sensing*, Rev. Mod. Phys. **89**, 035002 (2017).

[73] P. Maletinsky, S. Hong, M. S. Grinolds, B. Hausmann, M. D. Lukin, R. L. Walsworth, M. Loncar, and A. Yacoby, *A Robust Scanning Diamond Sensor for Nanoscale Imaging with Single Nitrogen-Vacancy Centres*, Nat Nano **7**, 320 (2012).

[74] B. K. Ofori-Okai, S. Pezzagna, K. Chang, M. Loretz, R. Schirhagl, Y. Tao, B. A. Moores, K. Groot-Berning, J. Meijer, and C. L. Degen, *Spin Properties of Very Shallow Nitrogen Vacancy Defects in Diamond*, Phys. Rev. B **86**, 081406 (2012).

[75] M. S. Wornle, P. Welter, M. Giraldo, T. Lottermoser, M. Fiebig, P. Gambardella, and C. L. Degen, *Structure of Antiferromagnetic Domain Walls in Single-Crystal Cr$_2$O$_3$*, ArXiv:2009.09015 [Cond-Mat, Physics:Quant-Ph] (2020).

[76] K. Chang, A. Eichler, J. Rhensius, L. Lorenzelli, and C. L. Degen, *Nanoscale Imaging of Current Density with a Single-Spin Magnetometer*, Nano Lett. **17**, 2367 (2017).

[77] A. Ariyaratne, D. Bluvstein, B. A. Myers, and A. C. B. Jayich, *Nanoscale Electrical Conductivity Imaging Using a Nitrogen-Vacancy Center in Diamond*, Nature Communications **9**, 1 (2018).

[78] D. Budker and M. Romalis, *Optical Magnetometry*, Nature Physics **3**, 4 (2007).

[79] G. Balasubramanian, P. Neumann, D. Twitchen, M. Markham, R. Kolesov, N. Mizuochi, J. Isoya, J. Achard, J. Beck, J. Tissler, V. Jacques, P. R. Hemmer, F. Jelezko, and J. Wrachtrup, *Ultralong Spin Coherence Time in Isotopically Engineered Diamond*, Nature Materials **8**, 5 (2009).

[80] G. de Lange, D. Ristè, V. V. Dobrovitski, and R. Hanson, *Single-Spin Magnetometry with Multipulse Sensing Sequences*, Phys. Rev. Lett. **106**, 080802 (2011).

[81] D. A. Hopper, J. D. Lauigan, T.-Y. Huang, and L. C. Bassett, *Real-Time Charge Initialization of Diamond Nitrogen-Vacancy Centers for Enhanced Spin Readout*, Phys. Rev. Applied **13**, 024016 (2020).

[82] S. A. Momenzadeh, R. J. Stöhr, F. F. de Oliveira, A. Brunner, A. Denisenko, S. Yang, F. Reinhard, and J. Wrachtrup, *Nanoengineered Diamond Waveguide as a Robust Bright*

852   *Platform for Nanomagnetometry Using Shallow Nitrogen Vacancy Centers*, Nano Lett. **15**, 165
853   (2015).

854 [83]   N. H. Wan, B. J. Shields, D. Kim, S. Mouradian, B. Lienhard, M. Walsh, H. Bakhru, T. Schröder,
855   and D. Englund, *Efficient Extraction of Light from a Nitrogen-Vacancy Center in a Diamond*
856   *Parabolic Reflector*, Nano Lett. **18**, 2787 (2018).

857 [84]   M. Lee, S. Jang, W. Jung, Y. Lee, T. Taniguchi, K. Watanabe, H.-R. Kim, H.-G. Park, G.-H. Lee,
858   and D. Lee, *Mapping Current Profiles of Point-Contacted Graphene Devices Using Single-Spin*
859   *Scanning Magnetometer*, Appl. Phys. Lett. **118**, 033101 (2021).

860 [85]   C. Gong, L. Li, Z. Li, H. Ji, A. Stern, Y. Xia, T. Cao, W. Bao, C. Wang, Y. Wang, Z. Q. Qiu, R. J.
861   Cava, S. G. Louie, J. Xia, and X. Zhang, *Discovery of Intrinsic Ferromagnetism in Two-*
862   *Dimensional van Der Waals Crystals*, Nature **546**, 7657 (2017).

863 [86]   S. Jiang, L. Li, Z. Wang, K. F. Mak, and J. Shan, *Controlling Magnetism in 2D CrI 3 by*
864   *Electrostatic Doping*, Nature Nanotechnology **13**, 7 (2018).

865 [87]   Z. Fei, B. Huang, P. Malinowski, W. Wang, T. Song, J. Sanchez, W. Yao, D. Xiao, X. Zhu, A. F.
866   May, W. Wu, D. H. Cobden, J.-H. Chu, and X. Xu, *Two-Dimensional Itinerant Ferromagnetism*
867   *in Atomically Thin Fe 3 GeTe 2*, Nature Materials **17**, 9 (2018).

868 [88]   C. Du, T. van der Sar, T. X. Zhou, P. Upadhyaya, F. Casola, H. Zhang, M. C. Onbasli, C. A. Ross,
869   R. L. Walsworth, Y. Tserkovnyak, and A. Yacoby, *Control and Local Measurement of the Spin*
870   *Chemical Potential in a Magnetic Insulator*, Science **357**, 195 (2017).

871 [89]   M. Jeffery, T. Van Duzer, J. R. Kirtley, and M. B. Ketchen, *Magnetic Imaging of Moat-guarded*
872   *Superconducting Electronic Circuits*, Appl. Phys. Lett. **67**, 1769 (1995).

873 [90]   T. Yamaoka, H. Tsujikawa, S. Hasumura, K. Andou, M. Shigeno, A. Ito, and H. Kawamura,
874   *Vacuum Magnetic Force Microscopy at High Temperatures: Observation of Permanent*
875   *Magnets*, Microscopy Today **22**, 12 (2014).

876 [91]   B. C. Stipe, H. J. Mamin, T. D. Stowe, T. W. Kenny, and D. Rugar, *Noncontact Friction and Force*
877   *Fluctuations between Closely Spaced Bodies*, Phys. Rev. Lett. **87**, 096801 (2001).

878 [92]   B. J. Roth, N. G. Sepulveda, and J. P. Wikswo, *Using a Magnetometer to Image a Two-*
879   *dimensional Current Distribution*, Journal of Applied Physics **65**, 361 (1989).

880 [93]   I. A. Beardsley, *Reconstruction of the Magnetization in a Thin Film by a Combination of*
881   *Lorentz Microscopy and External Field Measurements*, IEEE Transactions on Magnetics **25**, 671
882   (1989).

883 [94]   F. R. Braakman and M. Poggio, *Force Sensing with Nanowire Cantilevers*, Nanotechnology
884   (2019).

885 [95]   M. R. Koblischka, U. Hartmann, and T. Sulzbach, *Improving the Lateral Resolution of the MFM*
886   *Technique to the 10nm Range*, Journal of Magnetism and Magnetic Materials **272–276**, 2138
887   (2004).

888 [96]   L. Gao, L. P. Yue, T. Yokota, R. Skomski, S. H. Liou, H. Takahoshi, H. Saito, and S. Ishio, *Focused*
889   *Ion Beam Milled CoPt Magnetic Force Microscopy Tips for High Resolution Domain Images*,
890   IEEE Transactions on Magnetics **40**, 2194 (2004).

891 [97]   L. M. Belova, O. Hellwig, E. Dobisz, and E. Dan Dahlberg, *Rapid Preparation of Electron Beam*
892   *Induced Deposition Co Magnetic Force Microscopy Tips with 10 Nm Spatial Resolution*, Review
893   of Scientific Instruments **83**, 093711 (2012).

894 [98]   M. Jaafar, J. Pablo-Navarro, E. Berganza, P. Ares, C. Magén, A. Masseboeuf, C. Gatel, E.
895   Snoeck, J. Gómez-Herrero, J. M. de Teresa, and A. Asenjo, *Customized MFM Probes Based on*
896   *Magnetic Nanorods*, Nanoscale **12**, 10090 (2020).

897 [99]   B. Müller, M. Karrer, F. Limberger, M. Becker, B. Schröppel, C. J. Burkhardt, R. Kleiner, E.
898   Goldobin, and D. Koelle, *Josephson Junctions and SQUIDs Created by Focused Helium-Ion-*
899   *Beam Irradiation of* $\mathrm{Y}\mathrm{Ba}_2\mathrm{Cu}_3\mathrm{O}_7$, Phys. Rev. Applied
900   **11**, 044082 (2019).

901 [100]   S. Sangtawesin, B. L. Dwyer, S. Srinivasan, J. J. Allred, L. V. H. Rodgers, K. De Greve, A. Stacey,
902   N. Dontschuk, K. M. O'Donnell, D. Hu, D. A. Evans, C. Jaye, D. A. Fischer, M. L. Markham, D. J.

903 Twitchen, H. Park, M. D. Lukin, and N. P. de Leon, *Origins of Diamond Surface Noise Probed by*
904 *Correlating Single-Spin Measurements with Surface Spectroscopy*, Phys. Rev. X **9**, 031052
905 (2019).
906 [101] J. Martin, N. Akerman, G. Ulbricht, T. Lohmann, J. H. Smet, K. von Klitzing, and A. Yacoby,
907 *Observation of Electron–Hole Puddles in Graphene Using a Scanning Single-Electron*
908 *Transistor*, Nat Phys **4**, 144 (2008).
909 [102] J. A. Sulpizio, L. Ella, A. Rozen, J. Birkbeck, D. J. Perello, D. Dutta, M. Ben-Shalom, T. Taniguchi,
910 K. Watanabe, T. Holder, R. Queiroz, A. Stern, T. Scaffidi, A. K. Geim, and S. Ilani, *Visualizing*
911 *Poiseuille Flow of Hydrodynamic Electrons*, ArXiv:1905.11662 [Cond-Mat, Physics:Quant-Ph]
912 (2019).
913 [103] S. Schnez, J. Güttinger, M. Huefner, C. Stampfer, K. Ensslin, and T. Ihn, *Imaging Localized*
914 *States in Graphene Nanostructures*, Phys. Rev. B **82**, 165445 (2010).
915 [104] K. Lee, M. I. B. Utama, S. Kahn, A. Samudrala, N. Leconte, B. Yang, S. Wang, K. Watanabe, T.
916 Taniguchi, M. V. P. Altoé, G. Zhang, A. Weber-Bargioni, M. Crommie, P. D. Ashby, J. Jung, F.
917 Wang, and A. Zettl, *Ultrahigh-Resolution Scanning Microwave Impedance Microscopy of*
918 *Moiré Lattices and Superstructures*, Science Advances **6**, eabd1919 (2020).
919 [105] T. L. Quang, V. Cherkez, K. Nogajewski, M. Potemski, M. T. Dau, M. Jamet, P. Mallet, and J.-Y.
920 Veuillen, *Scanning Tunneling Spectroscopy of van Der Waals Graphene/Semiconductor*
921 *Interfaces: Absence of Fermi Level Pinning*, 2D Mater. **4**, 035019 (2017).
922 [106] A. Woessner, M. B. Lundeberg, Y. Gao, A. Principi, P. Alonso-González, M. Carrega, K.
923 Watanabe, T. Taniguchi, G. Vignale, M. Polini, J. Hone, R. Hillenbrand, and F. H. L. Koppens,
924 *Highly Confined Low-Loss Plasmons in Graphene–Boron Nitride Heterostructures*, Nature
925 Materials **14**, 4 (2015).

926